Large-Eddy Simulation of a Scramjet Strut Injector with Pilot Injection

Sebastian Eberhardt and Stefan Hickel

Abstract A scramjet is an air breathing jet engine for hypersonic flight, in which combustion takes place at supersonic flow velocity. Fast mixing of fuel and the compressed air flow is thus essential for the efficient operation. Because the penetration depth of fuel injection perpendicular to the main flow direction is very small, strut injectors that are positioned directly within the supersonic core flow are usually used in large chambers. We performed large-eddy simulations for a generic strut-injector geometry. The main objective of this paper is the analysis of the pilot injection for flame stabilisation.

1 Introduction

In a scramjet combustor, efficient and fast mixing of injected fuel with the surrounding airflow is essential to enable combustion during the very short residence time of the reactants in the combustion chamber. The penetration depth of fuel injection perpendicular to the main flow direction is very small. Therefore strut injectors are used in large chambers, which are positioned within the supersonic core flow. Depending on the flight Mach number, the conditions in a supersonic combustion chamber allow for autoignition of the fuel. The governing quantity for this process is the static temperature of the gas in the mixing region. If the flight Mach number is small, the temperature in the combustion chamber is also low, and not sufficient to ignite the fuel. Another scenario where autoignition may not be possible, depending on the setup, are ground experiments. To ignite the fuel, a pilot

S. Eberhardt
Institute of Aerodynamics and Fluid Mechanics, Technische Universität München, Boltzmannstr. 15, 85748 Garching, Germany
e-mail: sebastian.eberhardt@tum.de

S. Hickel (✉)
Institute of Aerodynamics and Fluid Mechanics, Technische Universität München, Boltzmannstr. 15, 85748 Garching, Germany

Faculty of Aerospace Engineering, Aerodynamics Group, Technische Universiteit Delft, P.O. Box 5058, 2600 GB Delft, The Netherlands
e-mail: S.Hickel@tudelft.nl; sh@tum.de

W.E. Nagel et al. (eds.), *High Performance Computing in Science and Engineering '15*, DOI 10.1007/978-3-319-24633-8_26

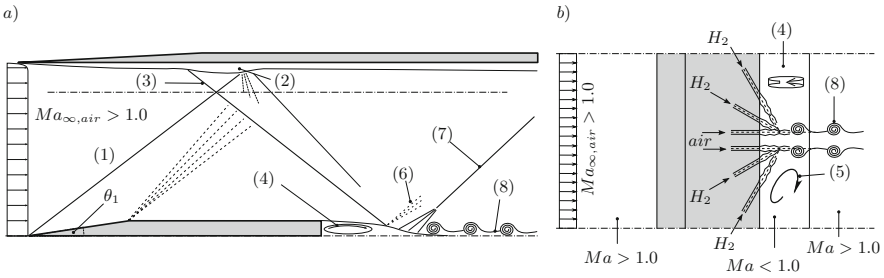

Fig. 1 Sketch of the strut injector pilot injection flow from the *side* (**a**) and *top* (**b**)

flame is then used. We present large-eddy simulation results for such a pilot flame. The strut-injector geometry is based on an experimental facilities at the Institute for Flight Propulsion of Technische Universität München. Fuel and oxidizer for the pilot flame are provided by several injections from the injector base. The main injection is switched off here to isolate effects belonging to the pilot flame. Results for the main injection of the same injector can be found in Eberhardt and Hickel [1].

Figure 1 provides an overview of the flow field: a primary shock (1) is generated by the sharp leading edge of the injector. This shock causes separation of the boundary-layer (2) and a separation shock (3) at the top wall. This reflected shock enters the recirculation region (4) following the strut's base where the shock is reflected as an expansion (6). Hydrogen and air is injected through six injectors at the base of the strut. A second, horizontal, recirculation (5) is created by the injection jets, which are oriented in such a way that the three jets of one side cross in a single point. Following the expansion, the recirculation collapses, creating a re-compression shock (7). In the wake of the injector a turbulent shear- and mixing-zone (8) is formed.

2 Experimental Setup

The combustion chamber used in the experiment was described by Fuhrmann [2] and is sketched in Fig. 2. It consists of a short section with parallel walls and a strut injector located in the middle of the channel. The strut injector has identical dimensions as the one investigated in [1]. Following the section with constant cross section is a diverging part with an opening angle of 5°. Fuel is injected through perpendicular nozzles on the strut injector's top and bottom. Optionally, hydrogen wall injectors in the divergent part of the chamber can be activated during operation. For the pilot injection, a total of six injections at the base of the injector are used. The two middle ones are parallel to the main flow direction and inject air, the other four are sloped in such a way that the hydrogen jets impinge on the air jets to enhance mixing. All pilot injectors have a diameter of $D = 0.5\,\text{mm}$. On the top wall of the chamber are bores for pressure taps to measure the wall pressure. The walls are made of copper with active water cooling to enable continuous operation without

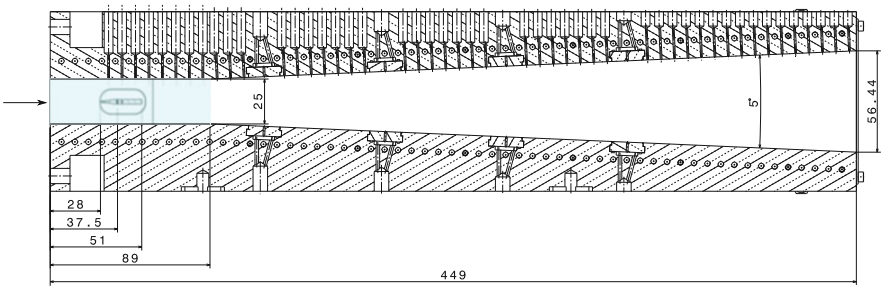

Fig. 2 Technical sketch as provided by Fuhrmann [2] of the experimental combustion chamber downstream from the laval nozzle. Highlighted in *blue* is the simulated section

overheating of the walls. The section with parallel walls measures $L_x = 89\,\text{mm}$ in x-direction, $L_y = 25\,\text{mm}$ in y-direction and $L_z = 27\,\text{mm}$ z-direction.

The air flow through the combustion chamber has a Mach number of $Ma_\infty = 2.15$ with a static temperature of $T_\infty = 509.2\,\text{K}$. The injection fluids both have a total temperature of $T_0 = 300\,\text{K}$. The total pressure can be calculated from the mass flow rate measured in the experiment. These mass flows are 0.25 g/s at both air injections and 22.5 mg/s hydrogen through each of the four hydrogen injectors. The resulting pressure values are $p_{0,inj,air} = 5.456 \cdot 10^5\,\text{Pa}$ for the air injectors and $p_{0,inj,H_2} = 1.857 \cdot 10^5\,\text{Pa}$ for the hydrogen injection.

3 Numerical Method and Computational Details

We solve the compressible multi-species Navier-Stokes equations (see [3], e.g.) with a finite-volume method on an adaptive Cartesian grid. The subgrid-scale (SGS) turbulence model is provided by the Adaptive Local Deconvolution Method (ALDM) of Hickel et al. [4, 5], which follows an implicit LES approach. ALDM is implemented for Cartesian collocated grids and used to discretize the convective terms of the Navier-Stokes equations. The diffusive terms are discretized by second order centered differences. The fully conservative cut-element immersed boundary technique of Örley et al. [6] is employed to represent the strut injector. For time-integration the explicit third order accurate Runge-Kutta scheme of Gottlieb and Shu [7] is used.

The LES in this study were performed using the flow solver INCA,[1] which is written in FORTRAN 2003. It uses a classical block-structured grid topology. For blocks which are not part of the same process, non-blocking communication according to the MPI standard[2] is employed, otherwise values are copied directly.

[1] http://www.inca-cfd.org.

[2] http://www.mpi-forum.org.

Three ghost-cell layers need to be exchanged as INCA uses discretization schemes that operate on six-cell stencils. Additional OpenMP directives allow a hybrid OpenMP/MPI parallelization, where several OpenMP threads share the workload assigned to one MPI process. The grid blocks can be distributed on an arbitrary number of MPI tasks, where the local blocks are stored in a linked list. Several load balancing strategies can be used to distribute the grid blocks: either INCA's internal partitioner that aims at balancing the computational load (total no. of cells per task) while minimizing the communication load (total no. of communicated data between tasks), or the more sophisticated METIS[3] library are possible choices.

To evaluate the scaling capabilities of INCA we performed a strong-scaling study on Hermit. The test problem is chosen to be a compressible Taylor-Green vortex and only one OpenMP thread per MPI process is used. We consider this the worst-case scenario. The computational domain is a cube with periodic boundary conditions in all directions. The domain is discretized by $N = 256^3$ cells with homogeneous grid spacing and the cube has an edge length of 2π on all sides. The domain is divided into subdomains of identical size according to the number of cores used, starting with 32 cores up to 2048. The number of cells per core, ghost cells per core, and ratio of ghost cells to cells is given in Table 1. Figure 3 shows the strong scaling

Table 1 Grid statistics for strong scaling of INCA

No. of cores	Cells/core	Ghost cells/core	Ghost cells/cells (%)
32	524,288	132,312	25.2
64	262,144	80,856	30.8
128	131,072	55,128	42.1
256	65,536	35,544	54.2
512	32,768	22,104	67.5
1024	16,384	15,384	93.9
2048	8192	10,200	124.5

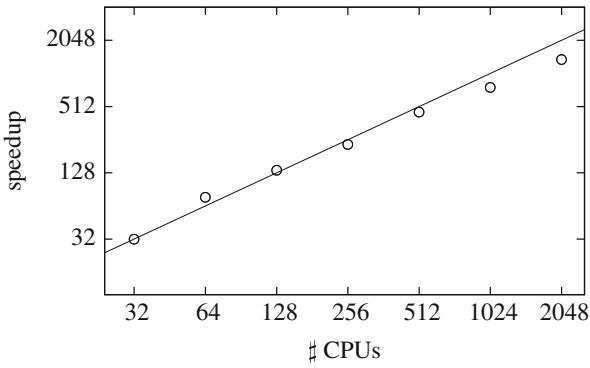

Fig. 3 Strong scaling of INCA on Hermit: speed-up on up to 64 nodes

[3] http://glaros.dtc.umn.edu.

on Hermit. For two and three nodes (64 and 128 cores), we observe a super-linear scaling that we attribute to optimized cache usage for these processor configurations. Up to the maximum investigated number of nodes, we observe good strong scaling properties of INCA. We conclude that an almost linear speed-up is possible by decomposing a computational grid into grid blocks with approximately 30,000 cells or more.

4 Numerical Setup

Figure 2 shows the computational domain and its position within the combustion chamber, which is the section with parallel walls and the strut injector. The inlet and outlet are supersonic boundary conditions. The four side walls are modeled as symmetries which corresponds to frictionless walls. These outer walls are not resolved to reduce computational costs and because the main focus of the study is the mixing zone in the wake of the strut. The injector surface and injection tubes are modeled as adiabatic walls by the immersed boundary technique [6]. Figure 4 displays a technical drawing of the experimental strut interior, (a) as given by Fuhrmann [2], and the wall created with the immersed boundary, (b), used in the simulations. The positions where injection boundary conditions are applied are pointed out as well. The boundary conditions applied for the injections is a total temperature and total pressure boundary condition.

For the calculation of the total pressure, the assumption (based on the Fanno flow) is made that the flow at the injection tube exit is critical. With this assumption

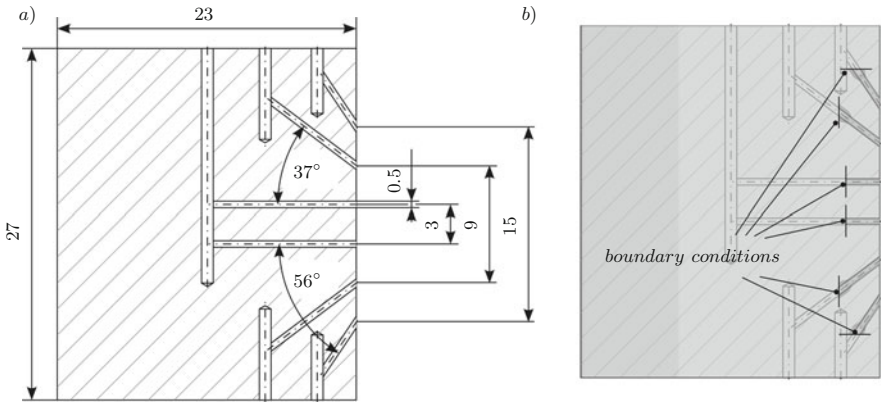

Fig. 4 (**a**) Technical drawing [2] of the experiments injector. (**b**) Representation of the injector geometry for the simulation, displayed by the immersed boundary wall as an overlay over the technical drawing

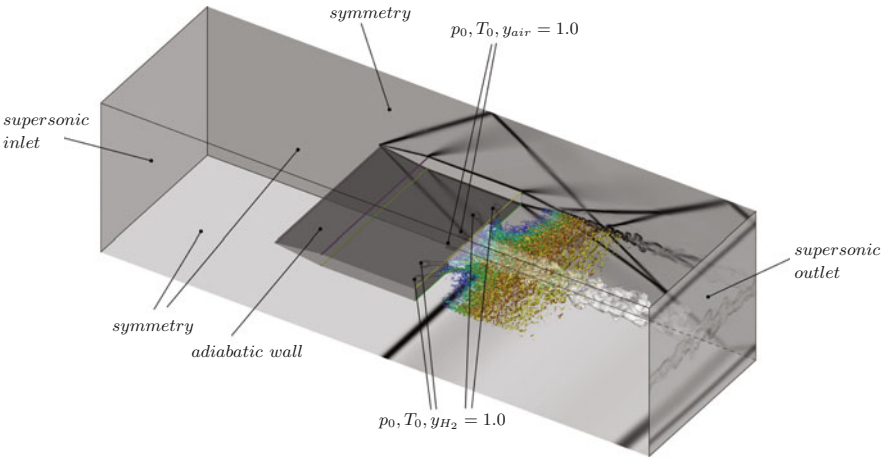

Fig. 5 Overview of the computational domain (including visualization of the flow) with applied boundary conditions. The origin of the computational frame of reference is the center of the injector's sharp leading edge

and the fact that the mass flow rate has a maximum at the point of critical flow, the total pressure for the boundary condition can be calculated:

$$p_0 = \frac{\dot{m}}{A}\frac{1}{\psi}\sqrt{\frac{RT_0}{2}},\ \psi = \left(\frac{2}{\gamma+1}\right)^{\frac{1}{\gamma-1}} \cdot \sqrt{\frac{\gamma}{\gamma-1}}. \tag{1}$$

We like to add that this functional only depends on the gas, the total temperature of the gas, the mass flow rate and the geometry of the tube. A summary of all boundary conditions used in this simulation is provided by Fig. 5.

The computational grid for this simulation consists of a total of 42 million cells with refinements around the injector wall on the outside and on the inside of the injection tubes. To capture the mixing zone, the wake of the strut is refined as well over a distance of 19 mm, which is almost one injector length. The grid has a homogeneous point distribution in z-direction. Figure 6 shows the grid topology and every fifth grid line.

5 Results

First we want to discuss the overall flow field around the strut injector. Figure 7 displays the instantaneous density gradient magnitude on a slice normal to the z-axis at a location $z = -0.0015$ m, which is the center of one of the air injections. The primary shocks from the injector leading edge are reflected at the top and bottom symmetries. They enter the recirculation region and increase the size of the subsonic

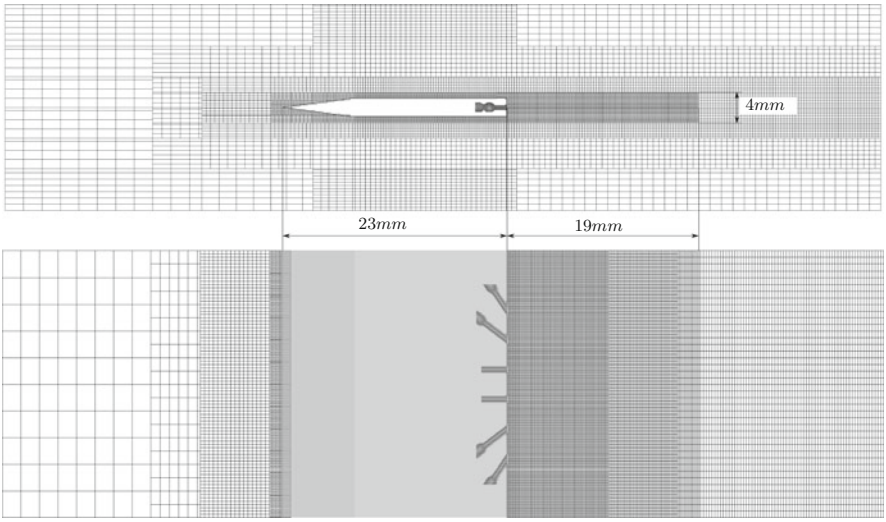

Fig. 6 Computational grid used for the simulation, displaying every fifth cell on a $z = 0.0$ (*top*) and a $y = 0.0$ (*bottom*) plane and an overlay of the immersed boundary

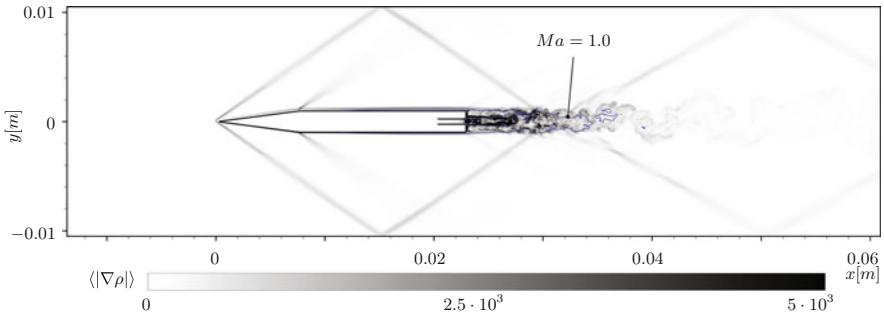

Fig. 7 Instantaneous density gradient magnitude on a $z = -0.0015$ m slice. This position cuts through one air injection at its center

region behind the injector base. From the base the injected supersonic air jet is visible which enters the recirculation. Following the recirculation re-compression socks are visible, as well as an unsteady, periodic shedding along the direction of the y-axis. The sonic line is added in Figs. 7, 8 and 9 to visualize the supersonic character of the injection jets and the region where the main flow re-accelerates to supersonic speed. Figure 8 displays a slice through the center of the strut at $y = 0$ slice. The Figure contains a graphical representation of the strut injector walls. Positions (*a*) through (*f*) mark the slice positions plotted in Fig. 9. The six injected jets and their super sonic region are clearly visible, with the two outer ones on each side impinging on the central jets. This creates a mixing region with strong

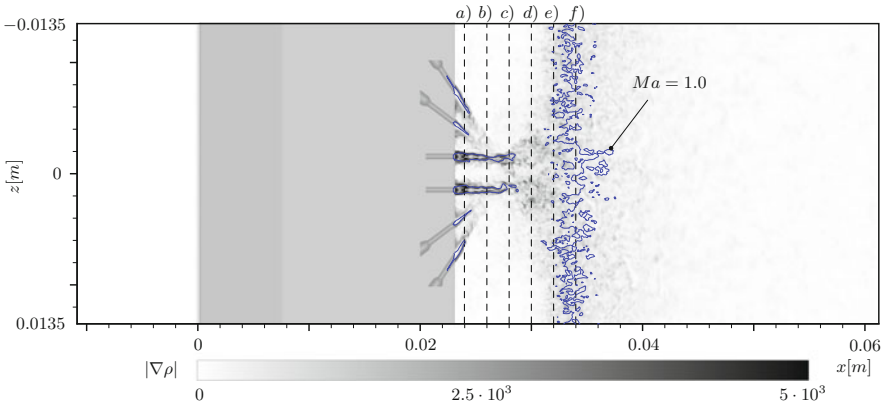

Fig. 8 Instantaneous density gradient magnitude on a $y = 0$ m slice including a $Ma = 1.0$ line and a geometric representation of the strut. Positions (**a**) through (**f**) mark the positions of slices in Figs. 9 and 15

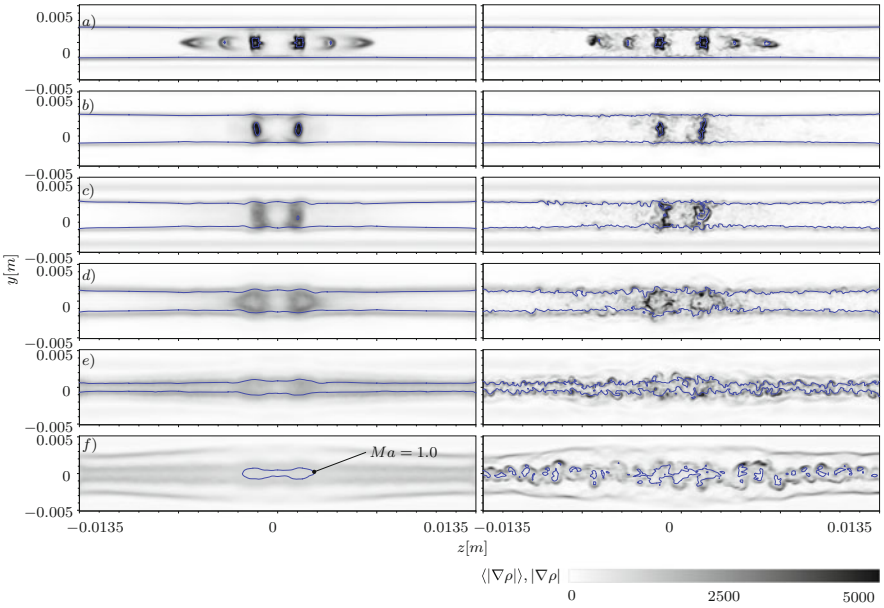

Fig. 9 Time averaged (*left*) and instantaneous (*right*) plots of the density gradient magnitude on slices with constant x-coordinate including a $Ma = 1.0$ line. The locations of the individual slices are marked in Fig. 8

turbulence within the subsonic recirculation behind the strut, which ensures a good mixture. The region $x \approx 0.034$ m indicates the re-acceleration to supersonic speed with presence of strong turbulence. The turbulence originates from the borders of the recirculation region, which collapses in this region. The same flow features

are visible in the instantaneous density gradient magnitude on the right hand side of Fig. 9. Close to the strut the degree of turbulence is low and increases with larger distance. The inner part around the jets is also turbulent near the injector, as they enter the recirculation with high speeds. Turbulence is further enhanced by the hydrogen jets impinging on the air jets although they are subsonic at the impingement point. In plot (c) the incoming shock from the top channel wall is visible and in plot (f) the re-compression shock, both as a horizontal dark bar. The air jets have the longest supersonic core, as they become subsonic only shortly before the main flow re-accelerates to supersonic speed. As the injected mass has to be accelerated in addition to the main flow, the subsonic region behind the air jets has the largest extend in x-direction as can be seen in the bottom left plot of Fig. 9. This figure also shows that, due to the added mass, the recirculation region in the wake becomes thicker in y-direction in the center of the flow.

The highest Mach number in the entire flow field is reached in the core of the air jets. Even though the Mach number there is higher than in the hydrogen jets, the absolute velocity in the hydrogen is higher due to the high speed of sound of the gas. The maximum Mach number in the air jets is around 2.65 and 1.4 in the hydrogen jets, as can be seen in Fig. 10. The sonic line in the same figure also shows a clear retardation in the x-direction following the air jets confirming the previous observation.

To analyze the mixing behavior of the injector, first the turbulence quantities variance of the velocity components, see Fig. 11, and turbulent kinetic energy, see Fig. 12, are analyzed. They are displayed in the figures on a slice at $y = 0$ m. These quantities show the edges of the injected jets to be the most turbulent part in the close wake of the injector. The air jets have the strongest variance in u direction due to the x-axis parallel injection, see Fig. 11a. Accordingly, the outer hydrogen jets create the largest fluctuations in w direction (z-axis) due to their large angle, see Fig. 11a. The largest turbulence intensity on the slice, however, is visible a short distance

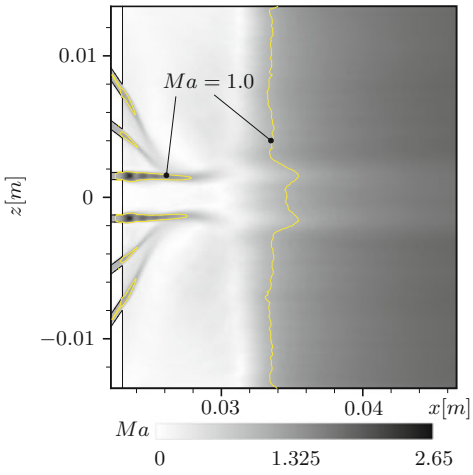

Fig. 10 Mach number on a $y = 0$ m slice in the wake of the strut including a $Ma = 1.0$ line

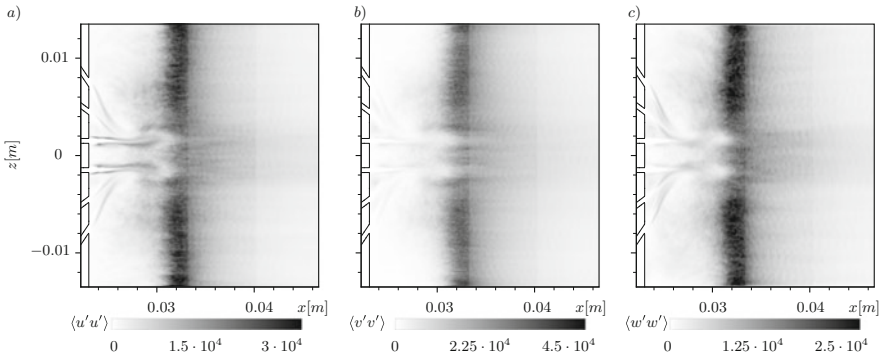

Fig. 11 Variance of the velocity fluctuations (**a**) $\langle u'u' \rangle$, (**b**) $\langle v'v' \rangle$ and (**c**) $\langle w'w' \rangle$ in all three directions on a $y = 0$ m slice

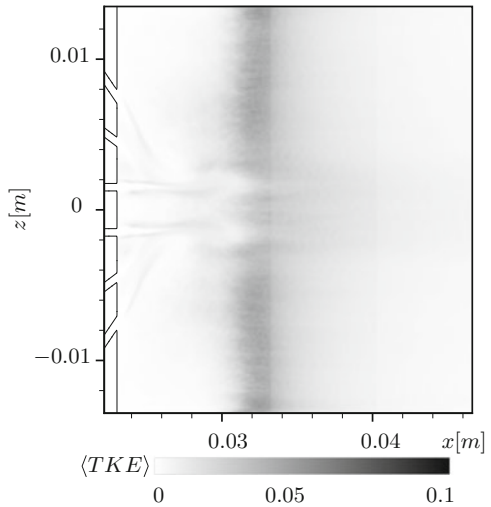

Fig. 12 Turbulent kinetic energy on a $y = 0$ m slice

downstream, where the flow re-accelerates to supersonic speed. This is again the region where the turbulence from the upper and lower border of the recirculation merge in the center of the flow. The shockwaves reflected from the upper and lower combustor walls hit the recirculation upstream of the maximum of turbulence and its trace can not be seen on the center slice.

The last of the turbulence statistic quantities considered here is the turbulent transport in the three directions, Fig. 13. It visualizes the mass transported by turbulence independent of the mass fractions of the mixing species. Again, the largest values of turbulent transport are visible in the x-direction (a) and z-direction (c). As expected, the vertical transport is the smallest on the symmetry plane. In

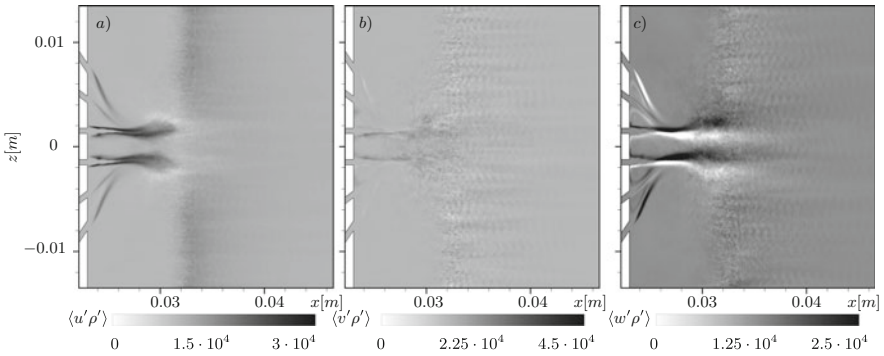

Fig. 13 Turbulent transport in all three directions on a $y = 0$ m slice

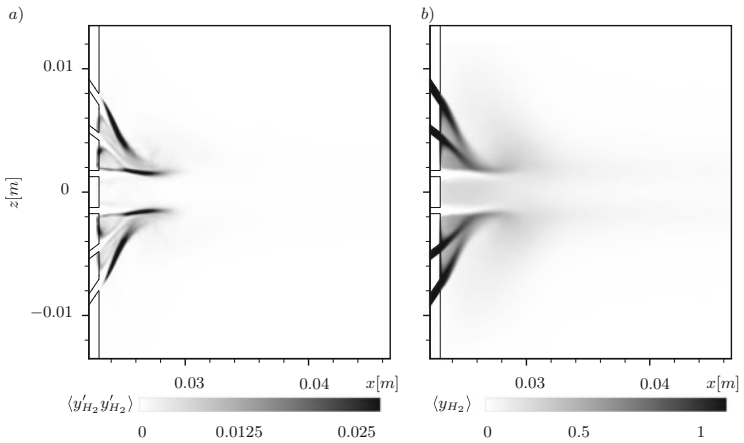

Fig. 14 Variance of the hydrogen mass fraction and hydrogen mean mass fraction on a $y = 0$ m slice

contrast to the variances discussed earlier, the region of highest turbulence is less pronounced in the turbulent transport. The region with the strongest transport again are the borders of the air jets, and the outer borders of the hydrogen jets.

The variance of the hydrogen mass fraction, Fig. 14a, supports the result of the velocity fluctuations as it shows maxima at the air jet boundaries where the hydrogen impinges, as well as on the outer boundary of the hydrogen jets. Furthermore, the figure shows that the six injection jets create two separated mixing zones, one on each side, with the most mixing on the outer boundary of the respective air jet. The mass fraction vanishes quickly because of the hydrogen's low density, and so there is no visible rise in mass-fraction variance in the region of high turbulence following the mixing. The mass fraction is plotted in Fig. 14b where the four jets are clearly visible. The region where the mass fraction spreads in z-direction at $x \approx 0.03$ m is caused by the horizontal recirculation. Following the region at $x \approx 0.032$ m the mass fraction is barely visible as it mixes with the air.

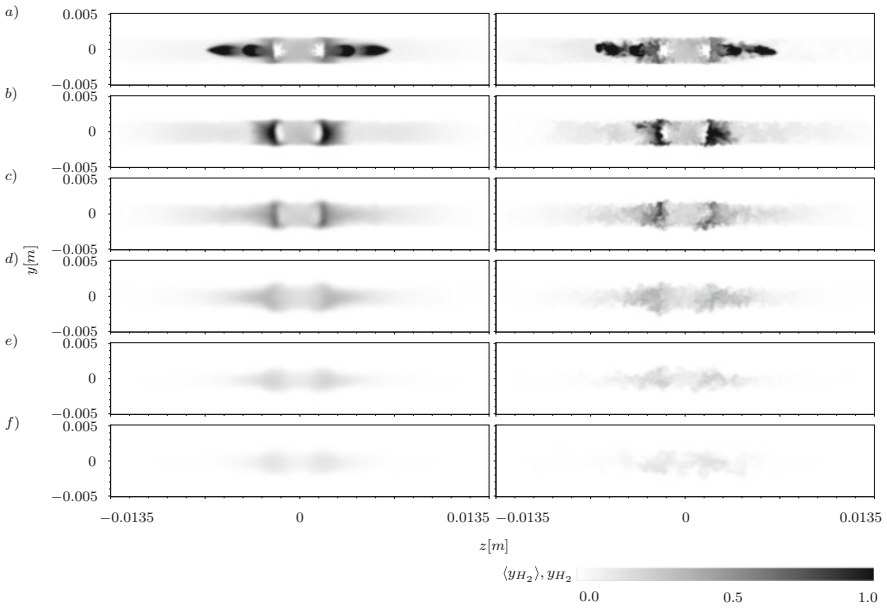

Fig. 15 Time averaged and instantaneous plots of the hydrogen mass fraction on slices with constant x-coordinate. The locations of the individual slices are marked in Fig. 8

A similar observation is made in Fig. 15. The plot shows the mean (left) and instantaneous (right) hydrogen mass fraction on $x = const.$ slices at the locations (a) through (f) as indicated in Fig. 8. The main regions of high mass fraction are located left and right of the air jets, which are clearly visible as white regions in the slices close to the injector. Further downstream the distribution becomes more homogeneous as the gases mix and the value of the H_2 mass fraction rapidly drops.

For hydrogen mixing the volume fraction gives additional information on the distribution and does not decay as quickly as the mass fraction. This can be seen in Figs. 16 and 17, where the mean volume fraction is shown. The first figure shows the density gradient magnitude in white to black contours and the volume fraction in white to blue at a position $z = -0.0015\,\text{m}$. The volume fraction is visible over the entire length of the domain following the injection and is spreading in spanwise direction further downstream. The region where the shocks from the channel walls hit the recirculation area shows a thickening due to the imposed upstream pressure gradient on the subsonic recirculation. Figure 17 displays the volume fraction distribution ranging from pure hydrogen on the one side of the color scale to pure air on the other side of the scale. Streamlines show the horizontal recirculation which enhances the mixing and is created by the hydrogen jets.

One of the goals of this study is to evaluate the pilot injection with respect to combustion and flame stabilization. The hydrogen volume fraction allows for a straight forward detection of the stoichiometric surface, which is a first

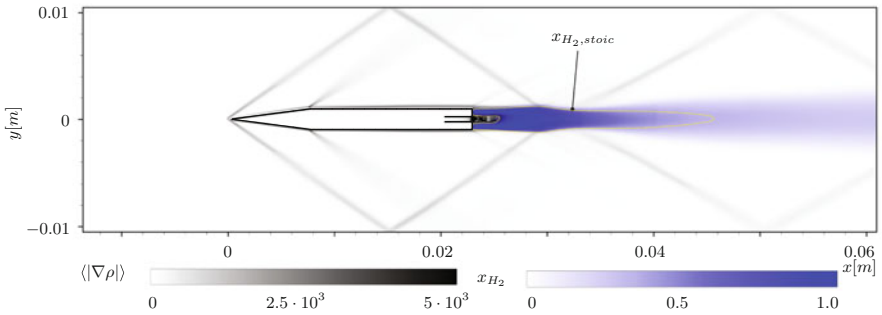

Fig. 16 Time averaged density gradient magnitude (*grey*) and hydrogen volume fraction (*blue*) on a $z = -0.0015$ m slice. *Yellow line* displays the stoichiometric line for hydrogen–air combustion

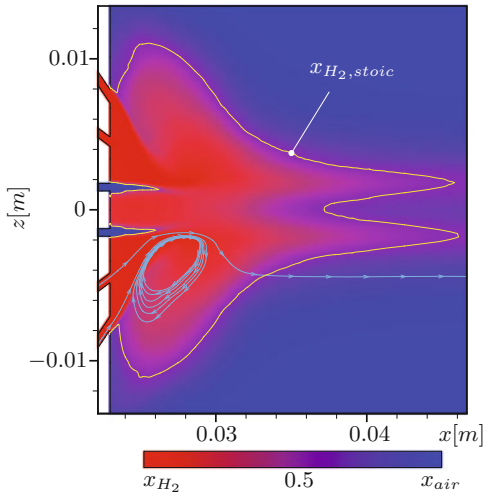

Fig. 17 Pure hydrogen volume fraction (*red*) to pure air volume fraction (*blue*) on a $y = 0$ m slice. *Yellow line* displays the stoichiometric line for hydrogen–air combustion

coarse approximation of the flame front location. The stoichiometric iso-line $x_{H_2,stoich} = 0.296$ for the combustion of hydrogen fuel with air has been added to Figs. 16 and 17 to give a rough estimate of where the main reaction zone will be. The large area of the stoichiometric surface indicates that the six hole pilot injector is a rather good solution for enabling ignition and for flame stabilization. Additionally, the subsonic recirculation region will have a higher temperature than the surrounding supersonic flow and the impinging oblique shock waves improve this even further.

Acknowledgements The support of this research within the Research Training Group "Aero-Thermodynamic Design of a Scramjet Propulsion System for Future Space Transportation Systems" 1095/2 by the Deutsche Forschungsgemeinschaft (DFG) and the High Performance Computing Centre Stuttgart (HLRS) is greatly acknowledged.

References

1. Eberhardt, S., Hickel, S.: Large-eddy simulation of a central strut injector with perpendicular injection for Scramjet applications. In: proceedings of 5th European Conference for Aerospace Sciences EUCASS (2013)
2. Fuhrmann, S., Hupfer, A., Kau, H.-P.: Investigations on multi-stage supersonic combustion in a model combustor. AIAA 2011–2332 (2011)
3. Tritschler, V.K., Zubel, M., Hickel, S., Adams, N.A.: Evolution of length scales and statistics of Richtmyer-Meshkov instability from direct numerical simulations. Phys. Rev. E 90, 063001 (2014). doi:10.1103/PhysRevE.90.063001
4. Hickel, S., Adams, N.A., Domaradzki, J.A.: An adaptive local deconvolution method for implicit LES. J. Comput. Phys. (2006). doi:10.1016/j.jcp.2005.08.017
5. Hickel, S., Egerer, C.P., Larsson, J.: Subgrid-scale modeling for implicit Large Eddy Simulation of compressible flows and shock turbulence interaction. Phys. Fluids **26**, 106101 (2014). doi:10.1063/1.4898641
6. Örley, F., Pasquariello, V., Hickel, S., Adams, N.A.: Cut-element based immersed boundary method for moving geometries in compressible liquid flows with cavitation. J. Comput. Phys. **283**, 1–22 (2015). doi:10.1016/j.jcp.2014.11.028
7. Gottlieb, S., Shu, C.-W.: Total variation diminishing Runge-Kutta schemes. Math. Comput. **67**, 73–85 (1998)